Proceedings of the INMM & ESARDA Joint Annual Meeting
May 22-26, 2023

Recent Advances in Uranium Particle Analyses by LG-SIMS

Evan Groopman[1], Todd Williamson[1], David Simons[2]

[1]Materials Measurement Science Division, National Institute of Standards and Technology, Gaithersburg, MD, 20899, USA
[2]MELE Associates, Inc., Rockville, MD, 20850, USA

Abstract

We present on the analysis of uranium particles by large-geometry secondary ion mass spectrometry (LG-SIMS) using three primary ion species, (O^-, O_2^-, O_3^-), and two sample substrates (graphite, silicon). The study shows that the primary species result in different magnitudes of mass fractionation, which are potentially driven by characteristics of the sputtering process and not by differences in the secondary ion energy distributions of U^+. O_3^- was found to yield consistently less mass fractionation across the secondary energy distribution compared to O^-. The shapes of the energy distributions do not account for the cumulative difference in fractionation. We also found that O_3^- improves the detection limits of ^{236}U compared to O^- by reducing the UH^+ signal for particles on a graphite substrate. The particle-to-particle hydride scatter was also reduced using O_3^-. We present on the development of an efficient, open-source Python tool, `FCpy`, for calculating Feldman-Cousins confidence intervals on low-count Poisson processes in the presence of a non-negligible, but known, average detector background signal. These methods and tools positively impact the analysis of environmental sampling and Nuclear Safeguards-related actinide particles. This work and other recent studies highlight important considerations for sample preparation and measurement design, particularly for inter-element analyses of individual atom-limited samples and separating different populations of particle data generated by large-area mapping.

1. Introduction

Large-geometry secondary ion mass spectrometry (LG-SIMS) is one technique used for identification and isotopic analysis of actinide particles related to Nuclear Safeguards and environmental sampling (Donohue, 1998; Axelsson et al., 2009; Ranebo et al., 2009; Hedberg et al., 2015; Hedberg et al., 2018). In many cases, individual particles and the isotopes of interest are atom-limited, where the achievable analytical precision and sensitivity are predominantly limited by ion counting statistics. Therefore, some of the most impactful analytical gains may be realized by increasing the total number of countable atoms through enhancement of the rate of secondary ion formation, by minimizing the magnitude of data post-processing corrections, and by incorporating statistical tools applicable to low-count data.

As an example, LG-SIMS is used to measure the isotopes of ^{234}U, ^{235}U, ^{236}U, ^{238}U from uranium particles. The measurement of $^{236}U^+$ (m/z = 236.046 u) by SIMS is obscured by an unresolvable isobaric interference from $^{235}U^1H^+$ (m/z = 236.052 u), which necessitates applying a correction based on the measured $^{238}U^1H^+/^{238}U^+$ ratio (Simons and Fassett, 2017). The intensity of the

uranium-hydride signal, and magnitude of the required correction, depend on the amount of hydrogen present in the SIMS sample vacuum chamber and on the characteristics of the sample substrate. The measurement's absolute uncertainty increases monotonically with the UH^+ signal intensity based on Poisson counting statistics, which subsequently increases the detection limits for ^{236}U. Therefore, reducing the hydride signal and the magnitude of the post-processing correction is important for maximizing sensitivity to ^{236}U. Here we present on new uranium hydride intensity data comparing the yields on carbon and silicon substrates under bombardment from O^-, O_2^-, and O_3^- ions.

SIMS uses a beam of "primary" ions that are focused onto the sample sputtering "secondary" ions, which can be measured, and neutral atoms, which are often redeposited on the substrate. The ratio of ionized/neutral atoms is typically less than a few %, though this is impacted strongly by the element of interest, the composition and structure of the material, and the primary beam characteristics, e.g., (Zinner, 1980; Wilson and Novak, 1991; Hervig et al., 2006). These factors, often collectively termed "matrix effects", also influence the relative sensitivity factors (RSF), or relative ionization rates, of different elements. For quantitative inter-element analyses of unknown samples, RSFs must be determined by measuring standards that match their composition and form, and under similar analytical conditions. For particle analyses, the RSF can change during the course of the analysis, so a majority of a particle must be consumed in order to reduce potential scatter (Szakal et al., 2019; Groopman et al., 2022). The molecular form of the primary ions (e.g., O_2^+, O^-, O_2^-, O_3^-) and optional oxygen flooding have also been shown to influence the RSFs and energy distributions for Pb/U (e.g., Schmitt and Zack (2012) and references therein) and Th/U (Groopman et al., 2022).

The National Institute of Standards and Technology (NIST) has recently developed new methods for acquiring and analyzing uranium particle data, which are expanded upon in this paper. Groopman et al. (2022) showed that by using O_3^- as the primary ion species instead of more conventional O^-, O_2^-, or O_2^+, the useful yields of uranium and thorium were increased by a factor of 1.9 ± 0.3, up to 4.7 % ± 0.4 % compared to 2.5 % ± 0.3 % for O^-. This compared favorably to previous measurements of the U^+ useful yield using LG-SIMS, which ranged between 1.0 % ± 0.1 % (O_2^+) and 1.7 % ± 0.1 % (O_2^-), with O^- intermediate (Ranebo et al., 2009; Sharp et al., 2016). O_3^- also had a 3× higher sputter rate than O^-, so the instantaneous ion yield was 5.6 ± 0.8 times higher in terms of ions · $(s \cdot nA \cdot \mu m^2)^{-1}$. Groopman et al. (2022) also investigated the influence of primary beam species and substrate composition on the RSF between Th^+ and U^+, instrumental mass fractionation, and production of molecular oxide ions. In summary, O_3^- primary ions were found to increase secondary ion yields (improving precision), reduce instrumental mass fractionation, and reduce the magnitude of matrix effects between particles on different substrates. Uranium isotope mass fractionation was found to be 2.6 ± 0.1 ‰/u for O^- and 1.5 ± 0.1 ‰/u for O_3^- when using a graphite substrate. It was speculated that this difference was due to the larger proportion of high-energy secondary ions under O^- bombardment. Here we report on further investigations into this difference.

Szakal et al. (2019) reported on the development of a radiometric particle age-dating method using the decay of ^{234}U to ^{230}Th ($t_{1/2}$ = 245,500 yr). Calculating a particle's model age requires precise knowledge of the Th/U RSF. In addition, the accuracy of the model age often depends upon

robust knowledge of the detector's average background count rate. For example, a one-year-old pure UO_2 particle with no initial ^{230}Th would have a $^{230}Th/^{234}U$ ratio of approximately 2.8×10^{-6}. The natural isotopic abundance of ^{234}U is approximately 0.0055 % and in NIST/NBL Certified Reference Material (CRM) U900 it is 0.778 ± 0.002 % (Croatto, 2014). Therefore, after one year, the absolute abundance of ^{230}Th in the particle with natural uranium composition would be 160 $pmol\cdot mol^{-1}$ and would be 22 $nmol\cdot mol^{-1}$ in a particle with composition matching U900. These are ultra-trace measurements, particularly when made on micrometer-scale particles. Therefore, analyses rely on statistical tools for interpreting the measurement of small signals in the presence of non-negligible detector background. Szakal et al. (2019) adapted a method from the high-energy physics community that was first proposed by Feldman and Cousins (1998) (FC). This method uses the known average background count rate and the observed total counts at m/z ≈ 230 to produce a Poisson process confidence interval (CI) about the value of the true ^{230}Th counts. This CI is converted to a count rate and combined with the ^{234}U count rate, RSF, and decay constant to produce a model age and associated CI. Here, we report on the development of an open-source software tool written in Python, `FCpy`, for calculating FC CIs that are useful for age-dating measurements (Groopman, 2022). The source code is available through NIST's GitHub webpage: https://github.com/usnistgov/FCpy.

2. LG-SIMS Methods

Isotopes of ^{235}U and ^{238}U were measured from CRM U900 under O^- or O_3^- primary ion bombardment using a Cameca IMS-1280 LG-SIMS (CAMECA Instruments, Inc., Fitchburg, WI, USA)[1]. Analytical conditions followed those employed for age dating and uranium isotopic measurements using the monocollector electron multiplier (EM) detector (Szakal et al., 2019; Groopman et al., 2022). In brief, a 50 µm primary Kohler spot was centered on each particle: 780 pA for O_3^- and 1.75 nA for O^-. An image field of 50 µm × 50 µm was used with a field aperture size of 6000 µm, which optically gated the acceptance region to 37.5 µm × 37.5 µm. A contrast aperture of 400 µm, entrance slit of 175 µm, and exit slit of 250 µm were used. The energy slit was reduced from the typical 50 eV width to 5 eV, and sample voltage offsets in 5 eV increments were applied between 0 eV and -35 eV (0 eV to 35 eV of initial kinetic energy). Isotopes of $^{235}U^+$ and $^{238}U^+$ were measured for 2.08 s and 4.96 s, respectively, over 40 cycles with wait times of 2.00 s and 0.96 s for magnet switching. Mass fractionation was calculated from the $^{235}U/^{238}U$ ratio at each voltage offset relative to the CRM U900 certificate values. Five to nine measurements were made for O^- and O_3^- at each voltage offset. The U900 particles were dispersed on a carbon planchet, and all used in this study had been previously sputtered for Th/U RSF measurements. Scans of the energy distributions were performed using a 10 eV energy slit width.

Isotope measurements of $^{232}Th^+$, $^{234}U^+$, $^{235}U^+$, $^{236}U^+ + {}^{235}U^1H^+$, $^{238}U^+$, and $^{238}U^1H^+$ were also made on particles of U900 following the exact procedure described in (Szakal et al., 2019; Groopman et al., 2022), i.e., as above, but with a 50 eV energy slit width and count times of 2.00 s,

[1] Certain commercial equipment, instruments or materials are identified in this paper to specify the experimental procedure adequately. Such identification is not intended to imply recommendation or endorsement by the National Institute of Standards and Technology, nor is it intended to imply that the materials or equipment identified are necessarily the best available for the purpose.

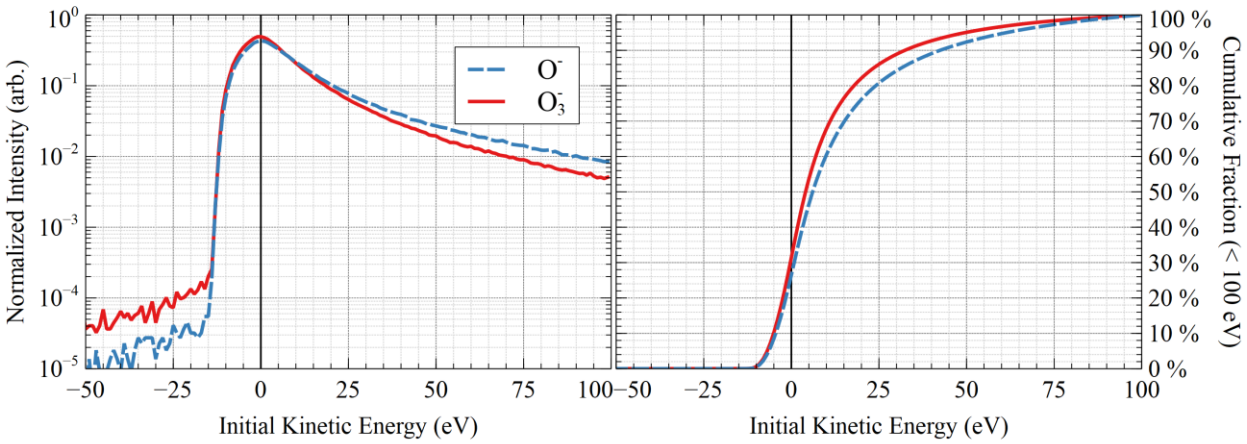

Figure 1: (left) Secondary ion energy distributions of U+ with a 10 eV energy slit width under O^- (dashed blue) and O_3^- (solid red) bombardment. O_3^- results in a narrower energy distribution. The intensities were normalized to the area under each distribution. (right) Cumulative energy distributions for ions with initial kinetic energies < 100 eV.

4.96 s, 1.04 s, 4.00 s, 3.04 s, and 4.00 s, respectively, over 20 cycles. All measurements were made following Th/U RSF measurements. The vacuum pressure in the sample chamber was approximately 1×10^{-8} Pa (1×10^{-10} mbar, 7.5×10^{-11} torr) during all analyses.

3. LG-SIMS Results and Discussion

Primary beam species O^-, O_2^-, and O_3^- have been shown to produce different U^+ energy distributions, with O_3^- having the largest proportion of lower-energy ions (Groopman et al., 2022). Figure 1 demonstrates this effect using a 10 eV energy slit, showing the distributions normalized to their areas on the left panel and the cumulative distributions of ions with initial kinetic energies less than 100 eV on the right panel. It was speculated that this difference may have influenced the trend in isotopic fractionation between the three species: decreasing from O^- to O_2^- to O_3^-. Figure 2 (left) shows the fractionation trends with respect to the secondary ion initial kinetic energy for O^- (blue triangles) and O_3^- (red squares) using a 5 eV energy window. Error bars show the standard error of the mean of the measurements at each offset voltage. Linear regressions (dashed lines) are shown to highlight the systematic difference between fractionation from O^- and O_3^- primary sputtering. Even at an initial kinetic energy near 0 eV, O^- yields higher mass fractionation than O_3^-. In the right panel, the ratios of O^-/O_3^- fractionation are shown at each offset. The raw average of the O^-/O_3^- ratio was 1.59 ± 0.27. Weighting the ratios by the relative proportions of ions at each point in the energy distributions shown in Figure 1 (left) yielded a mean O^-/O_3^- ratio of 1.70 ± 0.27 (shown). Both values agreed within uncertainty with the ratio of 1.73 ± 0.13 measured using a 50 eV energy slit width by Groopman et al. (2022), where fractionation from O^- was 2.6 ± 0.1 ‰/u and from O_3^- was 1.5 ± 0.1 ‰/u. Figure 3 shows the fractionation from O^- versus O_3^- for each offset with a linear regression and 1 σ confidence band on the fit. The regression yielded a slope of 1.12 ± 0.18 and a positive intercept of 0.52 ± 0.29. Therefore, we found no resolvable variation in the relative fractionation across the energy spectrum. O^- resulted in uniformly higher fractionation relative to O_3^-.

We conclude that the shapes of the secondary ion energy distributions do not explain the difference in the observed fractionation. For the earlier supposition to be correct, we would have expected to observe similar mass fractionation at low initial kinetic energy and diverging trends at

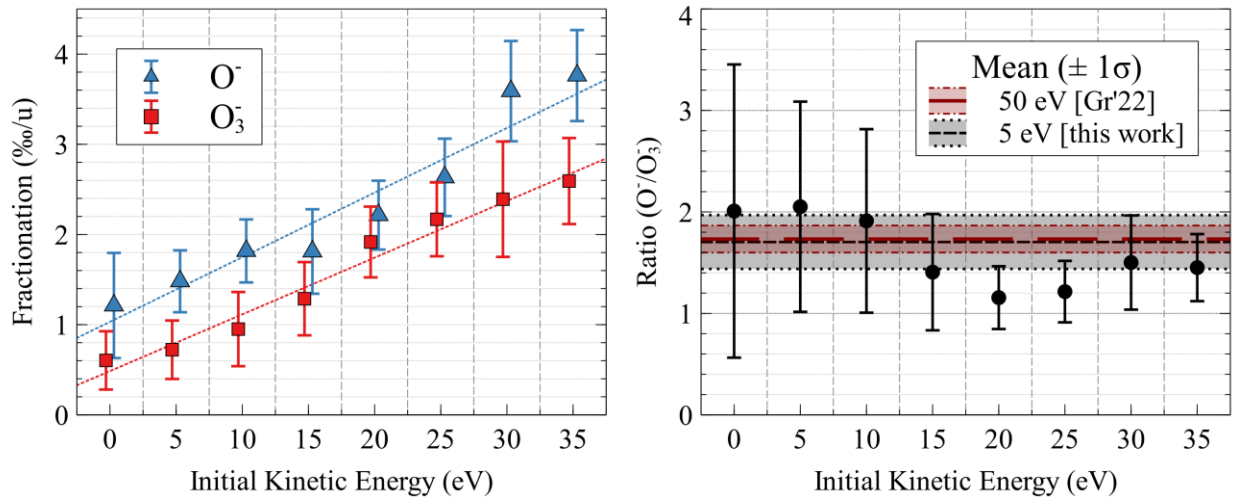

Figure 2: (left) Comparison of mass fractionation between O^- (blue triangles) and O_3^- (red squares). Regression lines to guide the eye. Qualitatively, there is a systematic offset between O^- and O_3^-. (right) The mean of the ratio values (1.70 ± 0.27) agrees with the measurement by Groopman et al. (2022) using a 50 eV energy slit (1.73 ± 0.13) [Gr'22].

higher offsets, with the magnitude of O^- fractionation increasing more rapidly than O_3^-. Since this was not the case and there was instead a uniform offset between the fractionation trends, it is likely that physical properties of the primary beam during the sputtering (such as implantation depth and impact energy density) were primarily responsible for the offset. The variance in energy distribution shapes only accounted for approximately 0.2 ± 0.4 ‰/u (unresolvable from zero) of the 1.1 ± 0.1 ‰/u difference between O^- and O_3^- fractionation shown in Groopman et al. (2022). Preferential sputtering of lighter isotopes under O^- bombardment could be a possibility, however, with SIMS it remains difficult to decouple ionization and sputtering effects since the neutral atoms removed from the sample cannot be measured.

Measuring the U isotope composition of a particle requires using the $^{238}U^1H^+/^{238}U^+$ ratio to correct for the isobaric interference of $^{235}U^1H^+$ with $^{236}U^+$, assuming that any isobaric interferences with $^{238}U^1H^+$ are negligible. Figure 4 shows a comparison of the $^{238}U^1H^+/^{238}U^+$ ratios for U900 particles measured with O^-, O_2^-, and O_3^- on graphite and silicon substrates. These measurements were all made following Th/U RSF measurements, used >10× the primary beam current and consumed most of the particle, so the hydride signals were lower than they would have been without pre-sputtering. The plots show the weighted mean of the data with two uncertainty values: one standard error of the weighted mean (SEM, shaded grey), and one weighted standard deviation (SD, lighter grey). On graphite, we observed a similar trend to the mass fractionation where the average UH^+/U^+ ratio was lowest for O_3^- and highest for O^-. The statistical uncertainties on each particle were 4.5 to 7.0 times smaller than the intrinsic particle-to-particle scatter, as shown by the mean square of the weighted

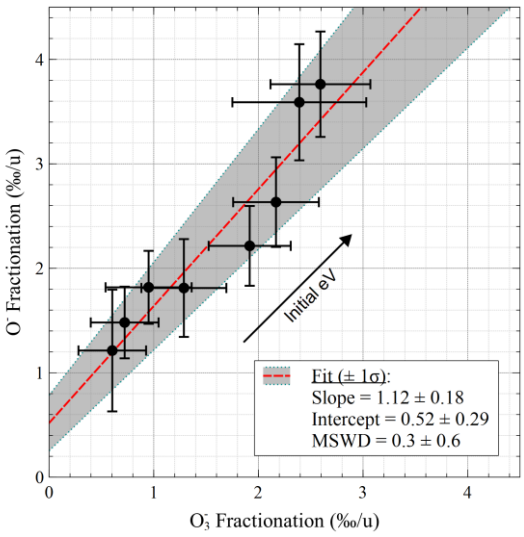

Figure 3: The magnitude of fractionation with respect to initial kinetic energy is correlated between O^- and O_3^-. However, O^- is offset systematically higher.

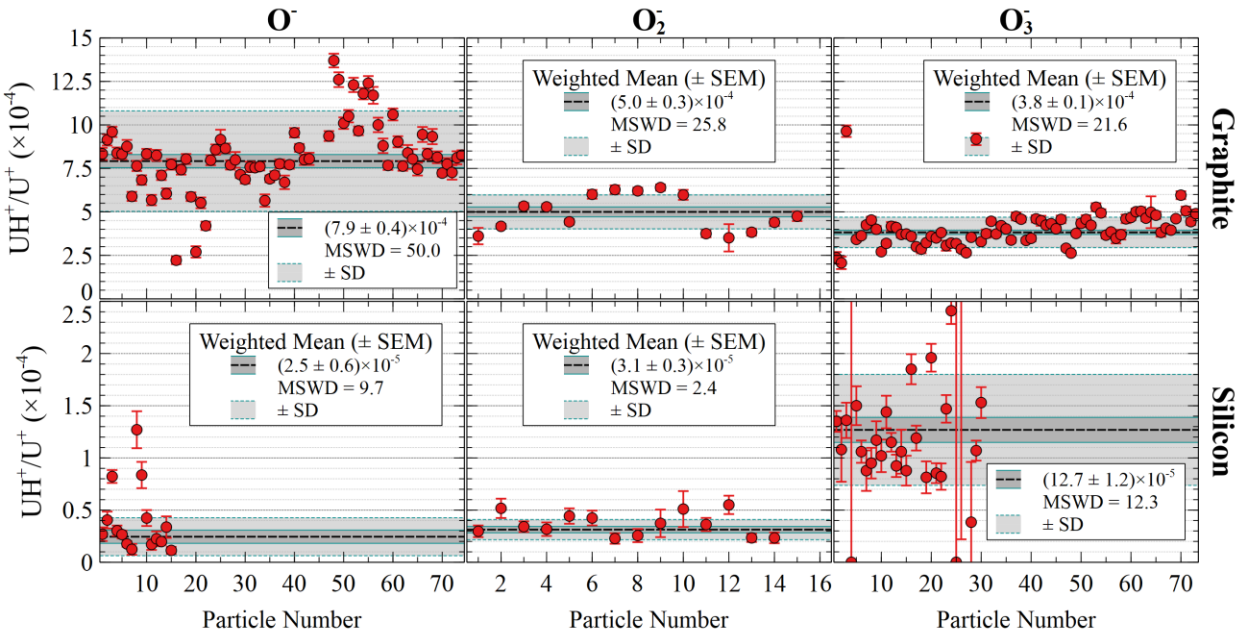

Figure 4: Comparison of UH^+/U^+ ratios between primary beam species and substrates. On graphite, O_3^- reduced the hydride ratio. O^- yielded the largest particle-to-particle scatter on both substrates. On graphite, the inter-particle scatter was on average 4.5 to 7.0 times the per-particle statistical uncertainties (√MSWD).

deviates (MSWD) values. The MSWD for the O^- data was much larger than for O_2^- and O_3^-, though the underlying cause was not immediately apparent. The data show that on average, O_3^- would be able to achieve an absolute uncertainty for ^{236}U of approximately 17 µmol·mol^{-1} compared to 21 µmol·mol^{-1} with O^- for a non-atom-limited particle with U900 composition (Simons and Fassett, 2017). These compare to 12 µmol·mol^{-1} and 13 µmol·mol^{-1} for O^- and O_3^- on Si. For an atom-limited particle, the relative useful yields would also be an important factor impacting the counting statistics uncertainties. However, as Simons and Fassett (2017) point out, there is little marginal improvement in the absolute detection limits for ^{236}U with hydride ratios below approximately 10^{-4}. Therefore, using O_3^- on graphite yielded a positive impact on the hydride ratio and ^{236}U detection limits, whereas it had limited negative impact on Si.

For the U900 on Si, we observed lower overall $^{238}U^1H^+/^{238}U^+$ ratios, in agreement with previous work (Simons and Fassett, 2017). All of the MSWDs from measurements on Si were several times lower than on graphite. We presume that most of the H available to form hydrides during analyses on graphite was from H intrinsic to the substrate itself, whereas on Si the H is more likely to be from adsorption from the vacuum and/or migration of H_2 and H_2O already on the substrate surface from exposure to air. Interestingly, the UH^+/U^+ ratios under O_3^- bombardment were approximately 5.1 ± 1.3 times higher than with O^-. This potentially indicates another difference in the physical and chemical sputtering process between primary beam species. Sputtering with O^- and O_2^- tends to oxidize the Si substrate into SiO_x ($x < 2$) once equilibrium ion implantation has been achieved (Wittmaack, 1996; Sharp et al., 2016; Groopman et al., 2022). This phase transition is readily apparent during depth profiling due to a characteristic jump in the instantaneous ion yield. In contrast, sputtering with O_2^+ and O_3^- produces smoother depth profiles that are not indicative of an abrupt phase transition. The data here may suggest that the phase-transitioned SiO_x surface under O^- and O_2^- bombardment may be less hydrophilic than the Si under O_3^-.

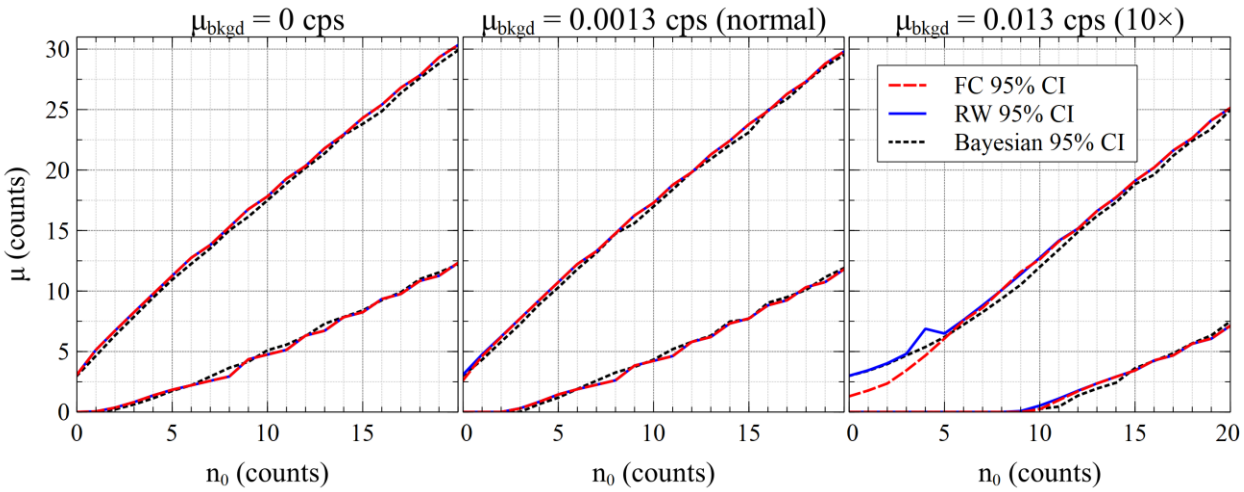

Figure 5: Comparison of 95% CIs calculated with different mean background levels over a 400 s measurement. The different methods broadly agree. The major difference appears at higher background levels, where the original FC method underestimates the CI upper limit for n_0 less than the expected number of background counts (right panel). The Bayesian and RW methods correct this (the RW implementation has a pathology at $n_0 = 4$ for unknown reasons).

These data show that under typical acquisition conditions for U-Th age dating and uranium isotopic analysis of particles, O_3^- yields the lowest hydride signal on a graphite substrate with respect to the other primary species and an elevated hydride signal on Si (though lower than all O_x^- species on graphite). For these analyses we did not attempt to minimize the hydride signal through sputter cleaning a larger area around the particles or using a cold finger within the vacuum chamber. Given the results for the hydride signal on Si under O_3^- bombardment, it would be worthwhile to explore the effects of primary beam current, which have been shown to influence the abundance of extrinsic H in the measured signal.

4. FCpy Software

Feldman-Cousins CIs (Feldman and Cousins, 1998) tend to be computationally expensive to calculate. This motivated the development of an efficient and fast open source program written in Python, `FCpy` (Groopman, 2022), so that the U-Th age dating analyses described by Szakal et al. (2019) could be easily reproduced by the community. `FCpy` takes as inputs the observed number of counts, n_0, the known mean background rate, b, the measurement time, t, and the desired confidence limit (e.g., 95%), and produces a CI for μ, the Poisson parameter. In words, the FC algorithm involves iterating over a finely spaced grid of potential μ values while calculating the Poisson probability mass function (which includes a factorial) for a range of counts, n. At each μ, the ratio of the Poisson likelihoods with and without $b \cdot t$ are computed and sorted. These sorted indices are used to compute an ordered sum of the probability mass function for μ up until summed probability reaches the confidence interval cutoff, e.g., 95%. The CI for μ, given n_0 and b, is then taken as the acceptance region where n_0 was among the range of n used to reach the CI cutoff. The variance of the Poisson distribution equals μ, so the range of n that must be checked increases for larger n_0. While it is beyond the scope of this paper to fully describe, there were additional corrections proposed to this algorithm, such as by Roe and Woodroofe (1999) (RW), that mitigated unwanted behavior such as the CI being reduced for large b when n_0 was small. For the case of zero observed total counts, it is clear that the observed number of background counts was also zero, so the effect

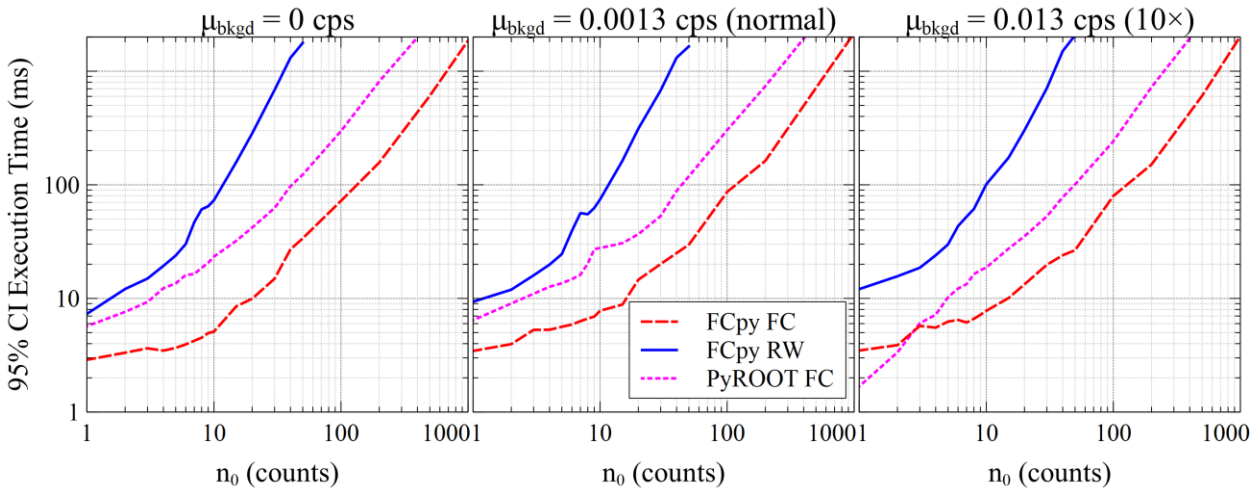

Figure 6: Execution times for `FCpy` calculating FC CIs on a Poisson process with and without the RW correction. Cases for average background rates of 0 cps (left), the long-term NIST average, 0.0013 cps (center), and 10× the NIST average, 0.013 cps (right) were evaluated for measurement times of 400 s. Most execution times were under 10 ms for low total counts, and below 100 ms for n_0 up to 100. The RW correction gets progressively more expensive as n_0 increases. The `FCpy` execution times also compare favorably to running the `ROOT` FC function using `PyROOT`.

of the mean background rate should not be incorporated into the final CI. However, such corrections effectively add a third dimension to the computational grid of μ and n values, iterating over a range of potential background counts, k, where k is limited to be less than n_0. `FCpy` includes an optional flag to turn on the RW correction.

Figure 5 shows the CIs calculated by the FC, RW, and a Bayesian method, for three levels of average background over a 400 s measurement. On the NIST LG-SIMS, the average monocollector EM background is approximately 0.0013 counts·s^{-1} (cps), or 0.52 expected counts over 400 s. There has been considerable review in the literature comparing the different methods, and this discussion is beyond the scope of this work, e.g., (Feldman and Cousins, 1998; Roe and Woodroofe, 1999; Roe and Woodroofe, 2000; Coakley et al., 2010). Figure 5 demonstrates that the three methods yield broadly similar results. The primary differences are illustrated in the right panel where the FC method underestimates the CI upper limit for n_0 less than the expected background counts. There is also an unusual pathology in the RW method for this background rate at $n_0 = 4$, though the cause remains unknown. The `FCpy` package also includes a Bayesian example model used for the calculations above, which requires the `PyMC` package and associated dependencies. At low count values ($n_0 \neq 4$) with high background, the upper limit of the RW method agrees with the Bayesian method, which intrinsically constrains the background counts to be less than or equal to n_0. `FCpy` also includes convenience functions for simultaneously calculating 68.3 %, 95 %, and 99.7 % CIs for a given n_0, b, and t; for calculating confidence bands as in Figure 5; and for fixing a mild pathology identified by Feldman and Cousins (1998).

`FCpy` leverages `numpy` and `scipy`, two core computational Python packages, and a high degree of vectorization and array broadcasting to eliminate explicit for loops from the calculations. These are the only two required dependencies. Benchmarks were run using the Python `timeit` module on a Dell Latitude 5420 laptop with Intel i7-1185G7 3.00GHz processor. Average runtimes were calculated by taking the total runtime of seven iterations of the function call and taking the mean of 3, 10, or 100 repetitions depending on the input n_0. Figure 6 shows a comparison of the execution

times. Three different background count rates were used for the FC (dashed red) and RW (solid blue) CIs. Automatic, conservative μ ranges were used for these benchmarks. For $n_0 < 10$, execution times were well under 10 ms per call for the FC limits and were under 100 ms per call for $n_0 < 100$. Having the user supply a more restrictive μ range reduced the runtime of the FC method for $n_0 = 500$ and $b = 0.0013$ from approximately 700 ms down to roughly 380 ms. The RW correction requires significantly more computation time, though for low-count scenarios where the correction actually has an interpretational impact, the runtimes were always less than 100 ms, down to approximately 7 ms in the best scenario. Note, as μ (n_0) gets larger, a Normal approximation to a Poisson likelihood becomes increasingly accurate, so using the FC or RW method for, e.g., $n_0 = 1000$, is unnecessary. The execution times are also favorable compared to using the `ROOT` data processing framework (Brun and Rademakers, 1997; Brun et al., 2019) through the `PyROOT` wrapper (dotted magenta). The FC algorithm has been coded in several other languages and this work is not meant to be an exhaustive comparison between most of them. It is only intended as a demonstration that for all reasonable values of n_0 and $b \cdot t$, the execution time of `FCpy` is unlikely to slow down a data processing pipeline for the analysis of many samples. As an additional comparison, the Bayesian method using `PyMC` (Salvatier et al., 2016) required approximately 15 s to sample 4 Markov chains with 5000 samples and 1000 tuning samples each on a single computer core for any n_0.

5. Conclusions

We reported on the results of investigations into the mechanisms of isotope fractionation and hydride molecule production in LG-SIMS for samples relevant to Nuclear Safeguards and environmental sampling. Smaller corrections and improved ion yields are important for maximizing the sensitivity and precision of uranium particle analyses. Following the work of Groopman et al. (2022), we found that there were considerable analytical benefits to using O_3^- primary ions for age dating and uranium isotopic analyses of individual particles. O_3^- resulted in lower mass fractionation than O^- and reduced the UH^+ signal on a graphite substrate. O^- resulted in significantly higher variance in the UH^+/U^+ ratios on graphite than the other primary beam species, on average approximately 7× larger than the statistical uncertainties on each measurement. Overall, the variance in the UH^+/U^+ ratios was larger on graphite than on Si. The fractionation differences between O_3^- and O^- were found to not be due to differences in the secondary ion energy distributions, implying that another mechanism related to primary beam interactions with the sample may be responsible. This work continues to highlight the importance of primary ion beam, sample, and substrate interactions and how they impact useful yields, precision, and isotope correction factors. These are important considerations for sample preparation and measurement design, particularly for inter-element analyses of individual atom-limited samples and separating different populations of particle data generated by large-area mapping.

References

1) Donohue D. L. (1998) Strengthening IAEA safeguards through environmental sampling and analysis. *Journal of Alloys and Compounds* **271**, 11-18.

2) Axelsson A., Fischer D. M. and Peńkin M. V. (2009) Use of data from environmental sampling for IAEA safeguards. Case study: uranium with near-natural 235U abundance. *Journal of Radioanalytical and Nuclear Chemistry* **282**, 725-729.

3) Ranebo Y., Hedberg P. M. L., Whitehouse M. J., Ingeneri K. and Littmann S. (2009) Improved isotopic SIMS measurements of uranium particles for nuclear safeguard purposes. *Journal of Analytical Atomic Spectrometry* **24**, 277-287.
4) Hedberg P. M. L., Peres P., Fernandes F. and Renaud L. (2015) Multiple ion counting measurement strategies by SIMS - a case study from nuclear safeguards and forensics. *Journal of Analytical Atomic Spectrometry* **30**, 2516-2524.
5) Hedberg P. M. L., Peres P., Fernandes F., Albert N. and Vincent C. (2018) Latest improvements in isotopic uranium particle analysis by large geometry-secondary ion mass spectrometry for nuclear safeguards purposes. *Journal of Vacuum Science & Technology B* **36**.
6) Simons D. S. and Fassett J. D. (2017) Measurement of uranium-236 in particles by secondary ion mass spectrometry. *J Anal At Spectrom* **32**, 393-401.
7) Zinner E. (1980) Depth Profiling by Secondary Ion Mass-Spectrometry. *Scanning* **3**, 57-78.
8) Wilson R. G. and Novak S. W. (1991) Systematics of Secondary-Ion-Mass Spectrometry Relative Sensitivity Factors Versus Electron-Affinity and Ionization-Potential for a Variety of Matrices Determined from Implanted Standards of More Than 70 Elements. *Journal of Applied Physics* **69**, 466-474.
9) Hervig R. L., Mazdab F. K., Williams P., Guan Y. B., Huss G. R. and Leshin L. A. (2006) Useful ion yields for Cameca IMS 3f and 6f SIMS: Limits on quantitative analysis. *Chemical Geology* **227**, 83-99.
10) Szakal C., Simons D. S., Fassett J. D. and Fahey A. J. (2019) Advances in age-dating of individual uranium particles by large geometry secondary ion mass spectrometry. *Analyst* **144**, 4219-4232.
11) Groopman E. E., Williamson T. L. and Simons D. S. (2022) Improved Uranium Particle Analysis by SIMS using O(3) (-) Primary Ions. *J Anal At Spectrom* **37**, 2089-2102.
12) Schmitt A. K. and Zack T. (2012) High-sensitivity U–Pb rutile dating by secondary ion mass spectrometry (SIMS) with an O2+ primary beam. *Chemical Geology* **332-333**, 65-73.
13) Sharp N., Fassett J. D. and Simons D. S. (2016) Uranium Ion Yields from Monodisperse Uranium Oxide Particles. *J Vac Sci Technol B Nanotechnol Microelectron* **34**.
14) Croatto P. (2014) U Series Reference Material Production, Age, and Sourcing. New Brunswick Laboratory.
15) Feldman G. J. and Cousins R. D. (1998) Unified approach to the classical statistical analysis of small signals. *Physical Review D* **57**, 3873-3889.
16) Groopman E. (2022) FCpy. https://github.com/usnistgov/FCpy.
17) Wittmaack K. (1996) Sputtering yield changes, surface movement and apparent profile shifts in SIMS depth analyses of silicon using oxygen primary ions. *Surface and Interface Analysis* **24**, 389-398.
18) Roe B. P. and Woodroofe M. B. (1999) Improved probability method for estimating signal in the presence of background. *Physical Review D* **60**.
19) Roe B. P. and Woodroofe M. B. (2000) Setting confidence belts. *Physical Review D* **63**.
20) Coakley K. J., Splett J. D. and Simons D. S. (2010) Frequentist coverage properties of uncertainty intervals for weak Poisson signals in the presence of background. *Measurement Science and Technology* **21**.
21) Brun R. and Rademakers F. (1997) ROOT - An object oriented data analysis framework. *Nucl Instrum Meth A* **389**, 81-86.
22) Brun R., Rademakers F., Canal P., Naumann A., Couet O., Moneta L., Vassilev V., Linev S., Piparo D., Ganis G., Bellenot B., Guiraud E., Amadio G., Wverkerke, Mato P., TimurP, Tadel M., Wlav, Tejedor E., Blomer J., Gheata A., Hageboeck S., Roiser S., Marsupial, Wunsch S., Shadura O., Bose A., CristinaCristescu, Valls X. and Isemann R. (2019) root-project/root: v6.18/02. *Zenodo* 10.5281/zenodo.3895860.
23) Salvatier J., Wiecki T. V. and Fonnesbeck C. (2016) Probabilistic programming in Python using PyMC3. *PeerJ Computer Science* **2**.